Tilting Pad Bearing Pivot Friction and Design Effects on Thermal Bow-Induced Rotor Vibration

Dongil Shin
Department of Mechanical Engineering,
Texas A&M University,
College Station, TX 77840
e-mail: davshin@tamu.edu

Alan B. Palazzolo
Professor
Department of Mechanical Engineering,
Texas A&M University,
College Station, TX 77840
e-mail: a-palazzolo@tamu.edu

The Morton effect (ME) is a thermally induced vibration problem observed in a rotor supported by hydrodynamic bearings. The journal's synchronous orbiting induces nonuniform viscous heating on its circumference, and the ensuing thermal bow often causes unacceptable vibration levels in the rotor. This paper investigates the influence of the tilting pad journal bearing (TPJB)'s pivot design on the severity and instability speed range of ME vibration. Simulations are conducted with two different types of pivots: cylindrical (CYL) and spherical (SPH), which produce different pad degrees-of-freedom and nonlinear pivot stiffness due to their geometries. The friction between pad and pivot, which only exists with the spherical pivot, is modeled, and its impact on the ME is evaluated. The example rotor model, as obtained from the literature, is single overhung, with experimentally measured excessive vibration and large journal temperature differentials, near 8000 rpm. The bearing and journal are modeled with three-dimensional (3D) finite elements, and the shaft with flexible beam elements for ME simulation. Nonlinear transient simulations are carried out for a wide operating speed range with varying pivot design parameters. Simulation results indicate that the predicted ME instability is sensitive to the pivot shape, pivot flexibility, and pad-pivot friction. [DOI: 10.1115/1.4050427]

Keywords: bearings, fluid film lubrication, friction, hydrodynamic lubrication, journal bearings, Morton effect, thermal bow vibration

1 Introduction

Many Morton effect (ME) instability cases have been reported in the past decade due to increased requirements for high operating speed and power in turbomachinery [1,2]. ME instability is mostly observed in overhung rotors equipped with fluid film bearings. Asymmetric oil viscous heating induces hot (highest temperature region in journal circumference) and cold spots (lowest temperature region in journal circumference) around the journal circumference. This temperature differential bends the rotor, producing increased inertial excitation in the system, and subsequently increased orbit size of the journal. This again develops more asymmetric journal heating for certain operating conditions. This cycle of asymmetric journal heating, thermal bow, and rotor vibration may form a positive feedback loop, which leads to spirally diverging or limit cycle vibration, and often stoppage of the machinery [1,3,4].

In 1993, Keogh and Morton [5] investigated journal differential heating with a theoretical model assuming steady, synchronous journal orbiting. The thermal bow amplitude of the shaft was predicted with a novel ME, rotor dynamic system model, that incorporated time-varying shaft bending and heat transfer [6]. de Jongh and Morton [3] analyzed a compressor with an overhung mass at its nondrive end (NDE) side, that experienced a high vibration level caused by the ME. The vibration was alleviated by changing the overhung mass at the NDE side. de Jongh and Van Der Hoeven [4] experimentally verified the ME instability in an overhung rotor exhibiting a high vibration level with substantial journal differential heating. A reduction in bearing clearance and applying a heat barrier sleeve between the journal and bearing suppressed the ME vibration. Lee and Palazzolo [7] used a Reynolds equation with variable viscosity, two-dimensional energy equation, and heat transfer models to predict the ME. Suh and Palazzolo [8,9] performed extensive parametric studies with a higher fidelity ME

model, utilizing three-dimensional (3D) energy equation heat transfer representation. The 3D thermo-hydrodynamic tilting pad journal bearing (TPJB) model utilized an equivalent mass imbalance to represent the thermal bow. Tong et al. [10] improved modeling fidelity by replacing the equivalent imbalance with a thermal bow model and including full 3D finite element method (FEM) models of the journal film and bearing. They also investigated the ME vibration in a double overhung rotor [11,12] and carried out extensive parametric studies with varying parameters of bearing clearance, oil viscosity, overhung mass, supply oil temperature, etc. The ME vibration in a gas-lubricated bearing was studied by the same authors [13]. A tilting pad gas bearing was developed based on 3D FEM, and the ME-induced spiral vibration similar to the oil-lubricated bearing was observed. They also experimentally verified the accuracy of the ME prediction model in the test rig where asymmetric journal heating was measured with 20 resistance temperature detector (RTD) sensors [14]. The measured temperature differentials were compared with both high-fidelity and simplified ME models and demonstrated the better prediction accuracy of the high-fidelity model. Shin and Palazzolo [15] investigated the effect of journal misalignment on the ME vibration. The same authors [16] used a squeeze film damper to suppress the ME-induced vibration problem. Simplified approaches to model and analyze the ME instability have been developed in Refs. [17–21]. Childs and Saha [17] developed an approximate algorithm for Morton effect prediction by calculating the shaft thermal gradient using temperature distributions from forward and backward whirl orbits. Murphy and Lorenz [18] presented an approximate Morton effect prediction method using the linear relationships among imbalance, vibration, and journal temperature. Kellenberger [19] suggested an analytical method to investigate the thermal bow vibration problem by considering the heat input to the shaft from rotor-stator rub. The method determines system stability by considering the ratio between heat input into the shaft and heat output from the shaft. Kirk et al. [20] developed an unbalance threshold approach for Morton effect analysis. This method uses the resultant imbalance (sum of mechanical and thermal imbalances) to determine the instability caused by the

Morton effect. Eckert and Schmied [21] suggested a method using hot spot stability to investigate Morton effect by adopting the hot spot model in Ref. [19].

Suh and Choi [22] conducted a dynamic performance comparison between the spherical (SPH) and cylindrical (CYL) pivots with a misaligned journal. The tilt, rolling, and yaw motions of a SPH pivot type were included, while the CYL pivot type only allowed the tilt motion due to its pivot geometry. The SPH pivot showed invariant bearing performance independent of the level of misalignment. Transient simulations of thermo-elastic-hydrodynamic TPJB have been researched by Gadangi et al. [23].

The dynamic characteristics of a TPJB are sensitive to its pivot design. The pivot acts as an elastic spring between the pad and housing and may significantly affect bearing characteristics such as lubricant film thickness, eccentricity ratio, damping, etc. A rigid pivot assumption is often used for simplicity, but this may result in a significant error in the bearing performance prediction. Prior studies [24–28] indicate the importance of considering pivot flexibility for accurate prediction of TPJB static and dynamic characteristics. The TPJB's nonlinear pivot stiffness was derived based on the Hertzian contact theory in Refs. [29,30], and its influence on dynamic coefficients was investigated in Ref. [31]. Shi et al. [32] investigated the effect of nonlinear pivot stiffness on the dynamic response of a Jeffcott rotor model. The nonlinear pivot significantly affected the predicted orbit size of the rotor, lubricant film thickness, and film pressure. The level of the influence varied with the amplitudes of static and dynamic applied loads.

Pad-pivot friction occurs in the SPH pivot type TPJB, where the pad slides over the pivot surface in response to journal motion. Pad-pivot friction has been the subject of many experimental and numerical studies. Wygant et al. [33,34] measured the dynamic coefficients of TPJBs with SPH pivots. The journal equilibrium position trajectory versus speed showed curved loci along with significant attitude angles, which confirms the existence of cross-coupled stiffness and damping due to pad-pivot friction. Pettinato and De Choudhury [35,36] measured the power loss, pad temperatures, and the equilibrium position of two TPJBs with different pivot types. Equilibrium positions with moderate attitude angles were identified for the SPH pivot TPJB, while negligible attitude angles were observed in the CYL pivot. Sabnavis [37] tested the SPH pivot TPJB, and their results showed that cross-coupled

stiffness and damping are present especially at low operating speeds and loads but reduce with increasing speed. Kim and Kim [38] established a mathematical model for pad-pivot friction and conducted numerical simulations, verifying that pivot friction significantly affects the pressure distribution and film thickness, and induced rotor instability. He [39] adopted a conformal contact model for the prediction of pivot-pad friction. Nonsynchronous pad vibration was induced by pivot friction, and the effect of pivot radius was investigated. Kim and Palazzolo [40] performed a nonlinear dynamic study of a SPH pivot TPJB, considering the pad-pivot friction effect. A Stribeck friction model [41] was used to include pad angular velocity-dependent, pivot friction coefficients (FC). Numerous nonlinear phenomena such as Hopf bifurcation, limit cycles, and nonsynchronous vibration appeared with both autonomous and nonautonomous conditions.

The effect of pivot friction on ME instability has not yet been thoroughly investigated. Although the effect of different pivot geometries was considered in Refs. [9,22], the pivots were frictionless. The analyses were also limited to the TPJB's static performance under misaligned journal conditions [22] and ME vibration using only linear pivot stiffness at a single operating speed [9]. The impact of pad-pivot friction under dynamic loading conditions was investigated in Refs. [38–40]. However, the ME was not considered, and their Jeffcott rotor model included only TPJB tilting motion, while SPH pivots allow both tilting and rolling motions. The present study considers the influence of pad-pivot design and friction on ME vibration, using more detailed models of pivots including nonlinear pivot stiffness, SPH pivot's rolling motion, and pad-pivot friction. An improved cooling effect of a SPH pivot compared with the CYL pivot is demonstrated. A time-varying, nonlinear pivot stiffness based on Hertzian contact theory is used, and its effect on ME is shown over a wide operating speed range.

2 Rotor-Bearing Modeling

2.1 Pad-Pivot Design. Both CYL and SPH type TPJB pivots are illustrated in Fig. 1. The former has a cylinder-shaped pivot on the backside of a pad. The CYL type only allows tilting motion, since the diameter of the pivot in the axial direction (pad rolling direction) is usually much larger than the one in the radial
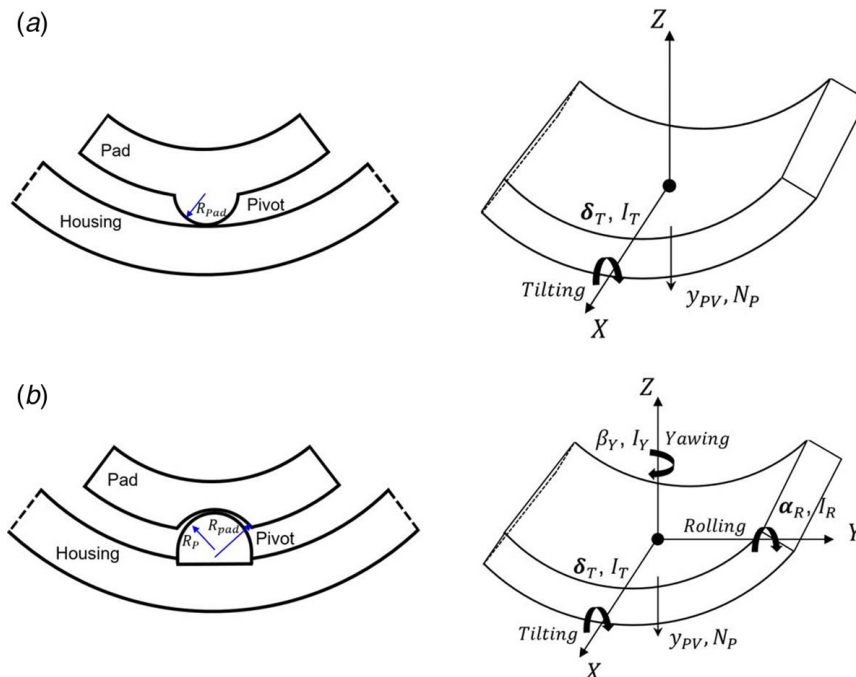

Fig. 1   Models of a (a) CYL type pad-pivot and (b) SPH type pad-pivot

direction, Meanwhile, since the SPH pivot has identical pivot diameters in both axial and radial directions, this pivot type enables both rolling and yawing motions, as well as tilting.

The nonlinear pivot stiffness is obtained from the Hertzian contact theory for each pivot type and used in the following simulations. From Refs. [29,30], the nonlinear pivot stiffness of the CYL type is expressed as

$$K_{CYL} = \frac{EL_{PIV}\pi}{2(1-\nu^2)\left(\frac{2}{3} + \ln\left(\frac{0.87EL_{PIV}(D_H - D_P)}{F_P}\right)\right)} \qquad (1)$$

where E and ν represent Young's modulus and Poisson's ratio of the pivot, respectively, and F_P is load applied on a pivot. The CYL pivot's axial length, housing diameter, and pivot diameter are L_{PIV}, D_H, and D_P, respectively. The nonlinear pivot stiffness of the SPH pivot [29,30] is expressed as

$$K_{SPH} = 1.442\sqrt[3]{\frac{F_P C_1}{C_2^2}}, \quad C_1 = \frac{D_{PH}D_P}{D_{PH} - D_P},$$

$$C_2 = \frac{1 - \nu_P^2}{E_p} + \frac{1 - \nu_{PH}^2}{E_{PH}} \qquad (2)$$

where F_P is load applied on a pivot, and D, ν, and E represent the diameter of pads and housing, Young's modulus, and Poisson's ratio, respectively. The subscripts P and PH represent the pivot and pivot housing, respectively.

Sliding friction occurs in the SPH pivot since the pad slides on the pivot as shown in Fig. 2. The mathematical model of pad-pivot friction developed in Ref. [38] is used in the current analysis. The friction force F_{FR} is determined by the product of the normal load applied on the pivot and the friction coefficient between two contact surfaces. The friction moment, M_{FR}, is the product of the pivot radius and the friction force, resists pad motion and is applied to each pad. Friction moments applied to the pads are separated into two categories, i.e. (1) sliding pad and (2) stuck pad

$$M_{FR} = -\frac{\dot{\delta}}{|\dot{\delta}|}|\mu_{FR}R_P W_{pad}| \text{ if } \dot{\delta} \neq 0$$

$$M_{FR} = \begin{cases} -M_P \text{ if } |M_P| < |\mu_{FR}R_P W_{pad}| \\ -\frac{M_P}{|M_P|}|\mu_{FR}R_P W_{pad}| \text{ if } |M_P| \geq |\mu_{FR}R_P W_{pad}| \end{cases} \qquad (3)$$

where $\dot{\delta}$ is the angular velocity of the tilting or rolling motion of the pads, μ_{FR}, R_P, and W_{pad} denote the friction coefficient, pivot radius, and load applied on the pad, respectively. M_P is an applied moment on the pad by the lubricant film pressure.

The friction moment is determined by multiplying the friction force ($F_{FR} = \mu_{FR}W_{pad}$) and the pivot radius (R_P), with its direction opposite to the pad motion, for the pad sliding case. If the pad is
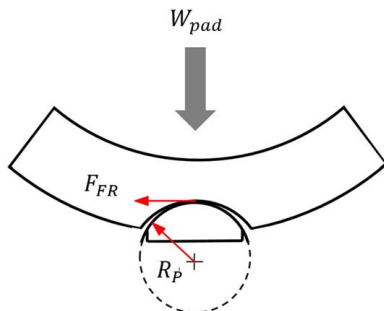
stuck, the friction exerts the moment with the same magnitude applied on the pad by the lubricant (M_P) up to the sliding value $\mu_{FR}R_P W_{pad}$. The direction of the friction moment is opposite to the external moment applied by the film on the pad. The angular velocity $\dot{\delta}$ can represent either tilting or rolling motion of the pad. Unlike prior work, which accounted only for the friction applied to pad tilting motion, the friction moment in both tilting and roll motions is included, while the friction due to yawing motion is assumed negligible. The friction moment during sliding is directed opposite to the resultant angular velocity of the pad. Note that a properly designed spherical pivot of a tilting pad bearing should not cause sliding friction between the pivot and housing; however, this does occur in practice. In fact, a pad may even become locked if the curvatures of the pivot and housing are not properly designed.

2.2 Reynolds and Energy Equations. Figure 3 shows the journal and a pad, where O_J and O_B are the centers of the journal and the bearing, respectively, and θ an θ_P denote the circumferential coordinate and angular position of the pivot, respectively.

The equation for lubricant film thickness in the case of the SPH pivot TPJB is

$$h(\theta, z) = C_P - \hat{e}_x \cos(\theta) - \hat{e}_y \sin(\theta) - (C_P - C_b)\cos(\theta - \theta_P)$$
$$- \delta_{tilt}R\sin(\theta - \theta_P) - h_{shaft \cdot TE}(\theta, z) - h_{pad \cdot TE}(h, z) \qquad (4)$$

where

$$\hat{e}_x = e_x - y_{pvt}\cos\theta_p - z\alpha_{rolling}\cos\theta_p - z\beta_{yaw}\cos(\theta_p + \pi/2),$$

$$\hat{e}_y = e_y - y_{pvt}\sin\theta_p - z\alpha_{rolling}\sin\theta_p - z\beta_{yaw}\sin(\theta_p + \pi/2)$$

C_P and C_b represent the pad and bearing clearances, respectively, y_{pvt}, δ_{tilt}, $\alpha_{rolling}$, and β_{yaw} denote the pivot displacement and tilting, rolling, and yaw motions, respectively, and R, $h_{shaft \cdot TE}$, and $h_{pad \cdot TE}$ are the journal radius, an thermal expansion of shaft, and pads, respectively.

The thermal expansion is obtained from 3D structural FEM as detailed in Refs. [8–10]. In the case of the CYL pivot, the terms related to rolling and yawing motions ($\alpha_{rolling}$ and β_{yaw}) in Eq. (4) are set to be zero. For the rigid pivot case, the pivot displacement y_{pvt} is also removed from the equation.

The generalized Reynolds and 3D energy equations are used to obtain the lubricant film force, including effects of variable viscosity. The Reynolds equation for an incompressible, Newtonian fluid, and negligible fluid inertia is

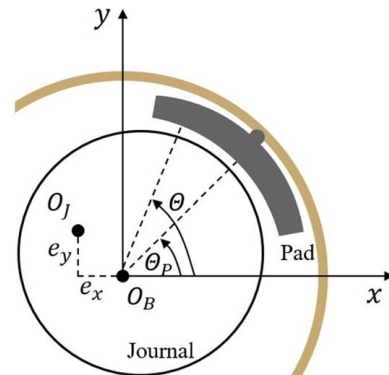$$\nabla \cdot (C_1 \nabla P) + \nabla D_2 \cdot U + \partial h/\partial t = 0$$

Fig. 2 Friction force between pad and pivot ($D_P = 2R_P$)

Fig. 3 Journal and pad locations and coordinates

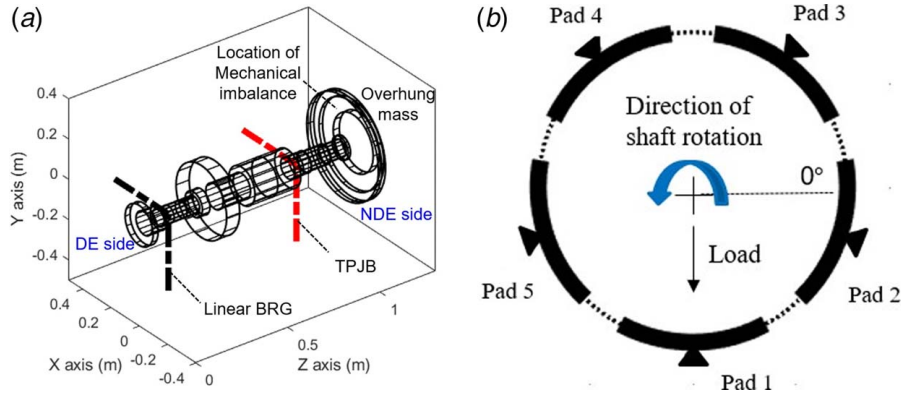**Fig. 4 Rotor and bearing configurations for the example model**

$$C_1 = \int_0^h \int_0^z (\xi/\mu)d\xi dz - C_2 \int_0^h (\xi/\mu)d\xi$$
$$C_2 = \int_0^h \int_0^z (1/\mu)d\xi dz / \int_0^h (1/\mu)d\xi$$

(5)

where h is lubricant film thickness, μ is a variable viscosity term dependent on lubricant temperature.

The viscosity–temperature relation is applied by

$$\mu = \mu_0 \exp^{-\alpha(T-T_0)}$$

(6)

where μ_0, T_0, and α are reference viscosity/temperature and viscosity coefficient, respectively, and T is the lubricant film temperatures obtained from 3D energy equation.

Film temperatures are obtained by solving the 3D energy equation

$$\rho c \left(u \frac{\partial T}{\partial x} + w \frac{\partial T}{\partial z} \right) = k \left(\frac{\partial^2 T}{\partial x^2} + \frac{\partial^2 T}{\partial y^2} + \frac{\partial^2 T}{\partial z^2} \right) + \mu \left[\left(\frac{\partial u}{\partial y} \right)^2 + \left(\frac{\partial w}{\partial y} \right)^2 \right]$$

(7)

where ρ, c, k, and μ are density, heat capacity, thermal conductivity, and lubricant film viscosity, respectively.

The temporal term is omitted from (7) since past studies demonstrated that its effects are negligible for thin film bearing application. The lubricant velocities in the circumferential direction (u) and axial direction (w) are obtained from the Reynolds Eq. (5). The Reynolds equation and energy equations are solved with the FEM, using 2D triangle elements for the former and 3D isoparametric hexahedron elements for the latter. A quadratic up-winding scheme [42] is applied for the FEM solution of the energy equation, to avoid spatial oscillations from the convection term in Eq. (7).

2.3 TPJB and Flexible Shaft Dynamics. The dynamic equations of the SPH pivot TPJB considering nonlinear pivot stiffness and pad-pivot friction are

$$m_{Pi} \ddot{y}_{PVi} = -K_{SPHi} y_{PVi} + F_{Pi}$$
$$I_{Ti} \ddot{\delta}_{Ti} = M_{Ti} + M_{FRi,T}$$
$$I_{Ri} \ddot{\alpha}_{Ri} = M_{Ri} + M_{FRi,R}$$
$$I_{Yi} \ddot{\beta}_{Yi} = M_{Yi} + M_{FRi,Y}$$

(8)

where i represents the pad number, and m_{Pi}, I_{Ti}, I_{Ri}, and I_{Yi} are the pad mass and pad inertia of tilting/rolling/yawing degrees of freedom, respectively.

The corresponding coordinates related to pad mass and inertia (y_{PVi}, δ_{Ti}, α_{Ri}, and β_{Yi}) are illustrated in Fig. 1. The nonlinear

pivot stiffness of the SPH pivot is K_{SPHi} and is calculated from Eq. (2). The stiffness value is time-varying since it is a function of the time-varying lubricant force applied on each pad (F_{Pi}). The pad-pivot friction moments, M_{FRi}, are applied to the relevant motions and axes. The friction moment for the yawing motion is assumed negligible and set to zero in the simulation. For the CYL pivot type, the degrees of freedom corresponding to rolling and yawing motions are removed, and the nonlinear pivot stiffness, K_{SPHi}, is replaced with K_{CYLi} in Eq. (1). This equation is combined with the Euler beam-flexible rotor model. The beam model is reduced with modal reduction and is combined with the tilting pad journal bearing equations in Eq. (8). A detailed explanation of this procedure is provided in Refs. [8,11]. Algorithms for solving the coupled, nonlinear ME equations are also provided in Refs. [8,11]. A procedure is presented for solving the coupled Reynolds, energy and thermal and dynamic structural equations of the rotor, and the TPJB. This utilizes a time-staggered, numerical integration algorithm to account for the large difference between thermal and vibration time constants in the transient ME.

3 Example

Figure 4 shows the rotor and bearing configurations used for the example ME simulation. A linear ball bearing and a nonlinear TPJB bearing are located at nodes 4 and 12, respectively, and an initial mechanical imbalance is located at the NDE overhung mass, node 18, in Fig. 4(a).

The total number of nodes in the shaft FEM model is 20. The stiffness and damping values of the linear ball bearing at node 4, and the magnitude of the mechanical imbalance are shown in Table 1. The TPJB with five pads and load-on-pad configuration is illustrated in Fig. 4(b). Parameters such as shaft diameter, lubricant properties, and TPJB design parameters are listed in Table 1. Design parameters for the two different pivot types, i.e., CYL and SPH pivots, used in the simulations are also provided in the table. The detailed rotor dimensions are provided in Table 2. The mechanical imbalance is attached at node 18, and the nonlinear TPJB force is applied at node 12.

3.1 Linear Analysis. Linear rotor dynamic unbalance response is first obtained based on bearing stiffness and damping coefficients, and pivot stiffness evaluated at journal equilibrium positions. The static load of 2170 N is applied to the TPJB bearing for both linear and nonlinear analyses. Results are presented at the TPJB (node 12) and rotor NDE end (overhung side, node 18) in Figs. 5(a) and 5(b). Linear unbalance indicates that both pivot types show almost identical vibration levels when a rigid pivot stiffness assumption is made. Pivot stiffness is shown in Figs. 5(c) and 5(d) with respect to operating speeds.

Table 1 Parameter values for the example system

Lubricant parameters		Bearing parameters	
Viscosity at 50 °C (Ns/m²)	0.0203	Pad type	Load on pad
Viscosity coefficients (1/°C)	0.031	No. of pads	5
Supply temperature (°C)	50	Radius of shaft (m)	0.0508
Inlet pressure (Pa)	1.32×10^5	Bearing clearance (μm)	74.9
Reference temperature (°C)	50	Preload	0.5
		Bearing length (m)	0.0508
Shaft parameters		Thermal expansion coefficient (1/°C)	1.3×10^{-5}
Heat capacity (J/kg °C)	453.6	Reference temperature (°C)	25
Heat conductivity (W/mK)	50	Pivot radius (mm)	15
Thermal expansion coefficient (1/°C)	1.22×10^{-5}	Pivot friction coefficient	0.1~0.4
Reference temperature (°C)	25	Linear ball bearing	
Thermal rotor length[a] (m)	0.3508	K_{xx}, K_{yy} (N/m)	1.7×10^8
		C_{xx}, C_{yy} (Ns/m)	1.0×10^5
Cylindrical pivot parameters		Spherical pivot parameters	
Pivot radius (mm)	20	Pivot radius (mm)	19.98
Pivot housing radius (mm)	62	Pivot housing radius (mm)	20
Length of cylindrical pivot (mm)	50.8	Elastic modulus of pivot (Pa)	2.1e11
Elastic modulus of pivot (Pa)	2.1e11	Poisson's ratio of pivot	0.3
Poisson's ratio of pivot	0.3		

[a]Length of the 3D FEM rotor model used for calculating shaft temperature and thermal bow. Seven times the journal length [8].

Table 2 Dimensions of rotor beam model

Rotor element no.	Element length (m)	Element diameter
1	0.02667	0.197612
2	0.077724	0.113538
3	0.054356	0.082296
4	0.06858	0.082296
5	0.06858	0.082296
6	0.041148	0.122428
7	0.07112	0.357378
8	0.148844	0.122428
9	0.12446	0.184404
10	0.12446	0.184404
11	0.046736	0.1016
12	0.04318	0.1016
13	0.108712	0.093472
14	0.085344	0.082296
15	0.0127	0.11303
16	0.019304	0.456057
17	0.019304	0.456057
18	0.019304	0.3904488
19	0.03302	0.282448

The critical speed of the rotor with nonlinear SPH pivots occurs at a lower speed around 6800 rpm, compared with the rigid SPH pivot case that shows the critical speed at 7800 rpm. The critical speed shift is more pronounced with the SPH pivots than the CYL pivots (7800 rpm →7500 rpm). This result is consistent with the results in Ref. [25], where the rigid pivot assumption significantly overpredicts the bearing's direct stiffness values and critical speeds.

The vibration levels at the TPJB in Fig. 5(a) increases compared with the rigid pivot case, while the vibration amplitude at the overhung location in Fig. 5(b) decreases significantly, when the nonlinear pivot is included. These results indicate that the nonlinear pivot stiffness changes the critical speed and also modifies the mode shape. Figures 5(c) and 5(d) show the stiffness of both pivot types versus speed. The stiffness of the SPH pivot (Fig. 5(c)) shows relatively low values ranging from 3.25×10^8 N/m to 4.5×10^8 N/m across the speed range while the CYL pivot (Fig. 5(d)) indicates higher pivot stiffness up to 1.7×10^9 N/m. The relatively softer pivot values with the SPH pivot explains the lower critical speed than the CYL pivot. The differences in pivot stiffness values for two pivot types is attributed to their geometries, and

the trend is similar to the results in Ref. [25]. The eccentricity ratios of the journal with different pivot types are presented in Figs. 5(e) and 5(f). As expected, higher journal eccentricities are predicted with the softer pivot types, i.e., higher eccentricity ratios with the nonlinear SPH than with the nonlinear CYL type.

3.2 Effect of Rigid Pivot Geometry on Morton Effect. Nonlinear ME simulations were conducted for different pivot designs and speeds. The Morton effect simulation with pivot friction effect encountered numerical errors when solved with a fourth–fifth-order Runge–Kutta solver with variable time-step. The numerical error was resolved by using a Runge–Kutta algorithm with a small fixed time-step of 1e-6. The accuracy of the fixed time method was also verified by comparing its results without friction with the results from the variable time-step method.

Figure 6 compares ME response quantities, between rigid CYL and rigid SPH pivot models. Rubbing between the rotor and bearing pads are assumed to occur when the minimum film thickness is less than 5% of the nominal pad clearance. Modeling of the rub condition response is beyond the scope of the present paper, since the machine would be tripped out of service under these conditions in an actual application. Therefore, the simulation stops when the minimum film thickness drops below 5%. Figure 6 shows nonlinear transient simulation results at 8600 rpm for both CYL and SPH rigid pivot types. Spiral vibration characteristic of the ME, are seen to occur in the 1× polar plot with slowly time-varying phase angle and amplitude at the journal location. The phase angle is referenced to each rotation cycle starting at coincidence of the initial mechanical imbalance with a fixed reference direction. The phase angle for the SPH pivot case changes continuously during the 30 min simulation time in Fig. 6(a), while the CYL case simulation is truncated when rubbing occurs at 4 min 32 s.

Figure 6(c) shows the time response for journal ΔT, defined as the difference between the maximum and minimum temperatures around the journal circumference. The high ΔT oscillations between 13 °C and 23 °C coincide with high vibration amplitude oscillations in Fig. 6(a), which is attributed to thermally induced shaft bow excitation. Rubbing was only observed with the CYL pivot case, although both pivot types have the same bearing stiffness, damping, and unbalance response in Fig. 5. This result is due to the pad rolling motion of the SPH pivot which provides an increased film thickness ratio, as compared with the CYL pivot. Thermal bow induces an asymmetric film distribution in the journal's axial direction, along with the circumferential direction. The
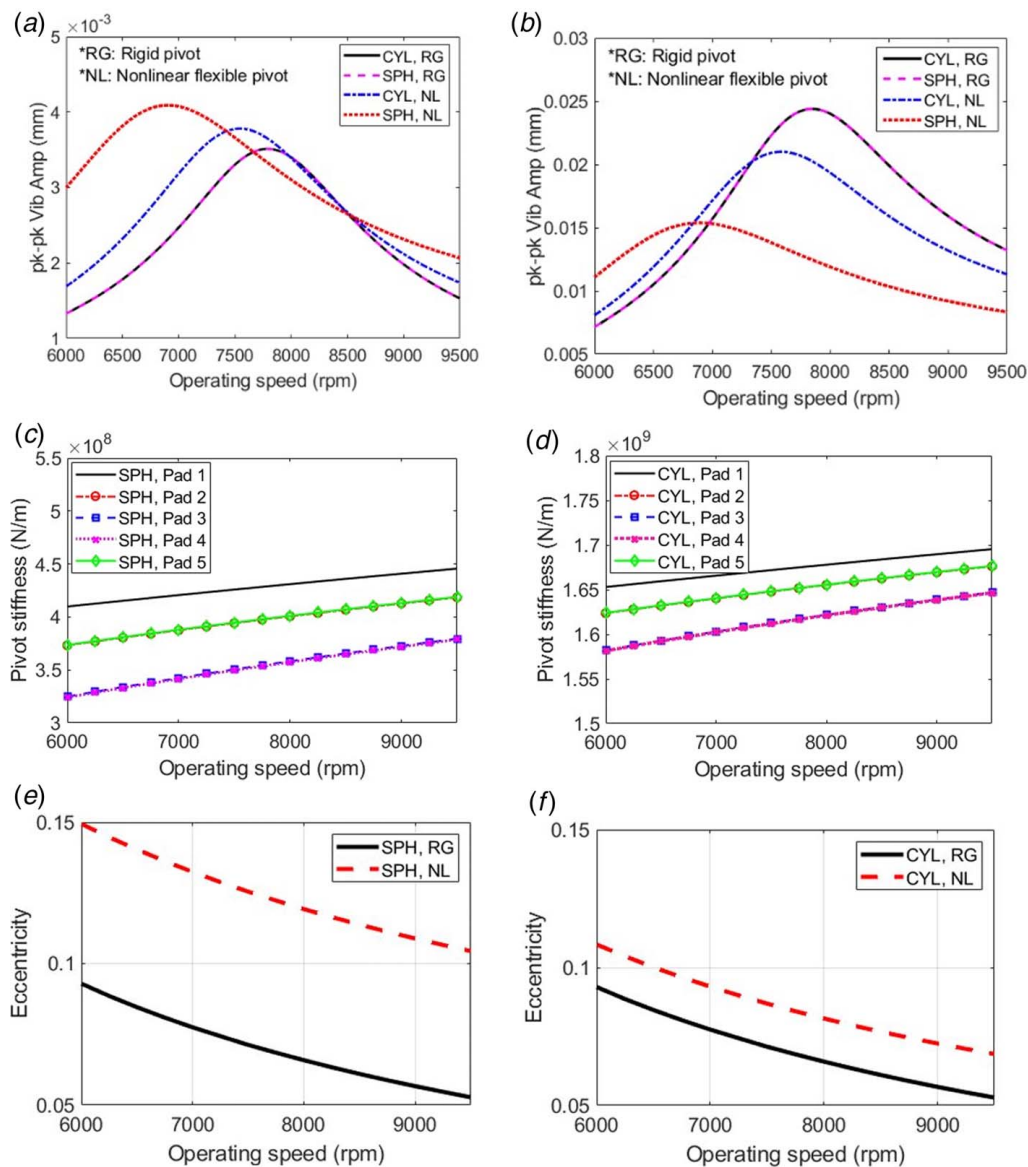
Fig. 5 Linear unbalance responses with different pivot types and flexibility: (a) at TPJB bearing, (b) at rotor NDE end, (c) equilibrium pivot stiffness of nonlinear SPH pivot case, (d) equilibrium pivot stiffness of nonlinear CYL pivot case, (e) eccentricity ratios of SPH type pivot (both rigid and nonlinear pivots), and (f) eccentricity ratios of CYL type pivot (both rigid and nonlinear pivots)

lubricant film thickness near the NDE side is smaller than the film near the DE side due to the larger thermal bow at the NDE. The SPH pivot's rolling motions in Fig. 6(d) compensates for the asymmetric film distribution in the axial direction, and thus relieves the rotor rub condition. Negative pad rolling angles occur in Fig. 6(d) for all five pads, due to the asymmetric pressure loading applied on the pads along the axial direction, which in turn produces more symmetric film thickness distributions. Fluctuations of pad rolling motions follow the vibration, film thickness and journal ΔT fluctuations as presented in Figs. 6(a), 6(b), and 6(c).

Figure 7 compares the journal temperature distributions for both pivot types at 4 min and 32 s. The vertical axis in the figure corresponds to the axial location of the journal in the shaft (from 0.8276 m to 0.8776 m). The temperature of the SPH pivot in Fig. 7(a) shows relatively symmetrical temperature distribution along the axial direction due to its rolling motion ability, while a more asymmetric distribution appears for the CYL case in Fig. 7(b), as the temperature of the NDE side is higher than the DE side temperature. The asymmetric heating in Fig. 7(b) is caused by the induced thermal bow effect which decreases the

film thickness at the NDE side more than the DE side. This causes the CYL pivot system to be more prone to rotor rubbing than the SPH pivot system.

3.3 Effect of Flexible Pivot Geometry on Morton Effect.
Figure 8 shows steady-state responses obtained from nonlinear transient integration, for both rigid and flexible pivot models, from 7000 rpm to 9500 rpm. Steady state here refers to 3 values: the clearance when the journal diverges to a rub condition, the peak value of a slowly varying, oscillatory vibration amplitude, or a constant asymptotic value. The flexible nonlinear CYL pivot shifts the ME instability speed range lower, similar with the linear unbalance results (Fig. 5), where the peak vibration speed was shifted lower when the rigid pivot is replaced with a flexible nonlinear pivot. For the rigid CYL pivot case, increasing high vibration appears between 8000 rpm and 9100 rpm. In contrast, increasing high vibration occurs between 7800 to 8600 rpm for the nonlinear pivot case. The unstable ME speed range is slightly reduced with the nonlinear pivot stiffness, i.e., an instability speed rage of
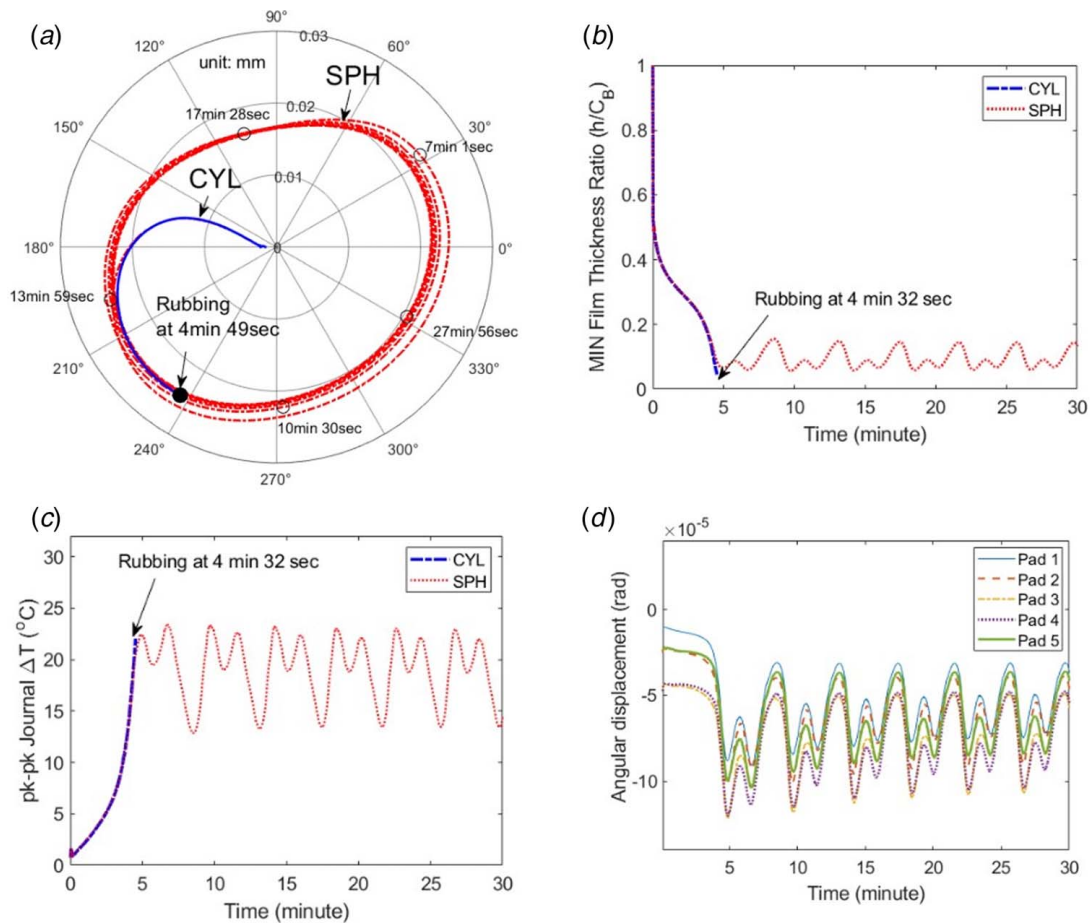
Fig. 6 Transient ME simulation at 8600 rpm for rigid pivots: (a) 1× vibration polar plot at journal location, (b) minimum film thickness ratio of the TPJB, (c) pk-pk Journal ΔT, and (d) pad rolling angular displacement for the SPH case

1100 rpm for the rigid pivot case and 800 rpm for the nonlinear, flexible pivot case.

Inspection of the cases in Fig. 8 suggests that the shift of the ME speed range due to the flexible nonlinear pivot is more apparent in the SPH pivot than the CYL one. This observation is consistent with the corresponding critical speed changes in the linear unbalance response in Fig. 5. There the critical speed shift is more significant with the SPH pivot compared with the CYL pivot, due to the CYL being stiffer than the SPH pivot.

Inspection of the pivot stiffness effects implies that the ME instability speed range is significantly affected by critical speed changes, as suggested by the ME instability speed shifts with different pivot stiffness values, and the corresponding critical speed changes. However, the ME is not a strict resonance problem as demonstrated by (1) many reported ME cases occurring distant from the rotor's critical speed and (2) ME vibration level at the speed closer to the critical speed not being more severe than at a speed more remote from the critical speed. For example, in Fig. 8(b), the vibration level of the rigid CYL case at 8600 rpm is higher than at 7700 rpm, where the critical speed occurred in the linear analysis in Fig. 5.

Figure 9 shows the journal temperature differential (ΔT) versus rpm and rotor axial location. Both SPH rigid pivot (Fig. 9(a)) and SPH nonlinear flexible pivot (Fig. 9(b)) cases are shown. High
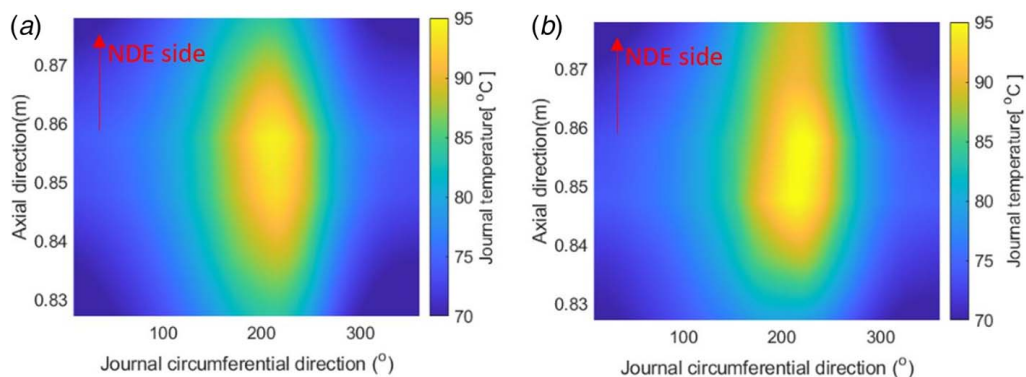

Fig. 7 Journal temperature at 8600 rpm (4 min 32 s): (a) SPH pivot and (b) CYL pivot
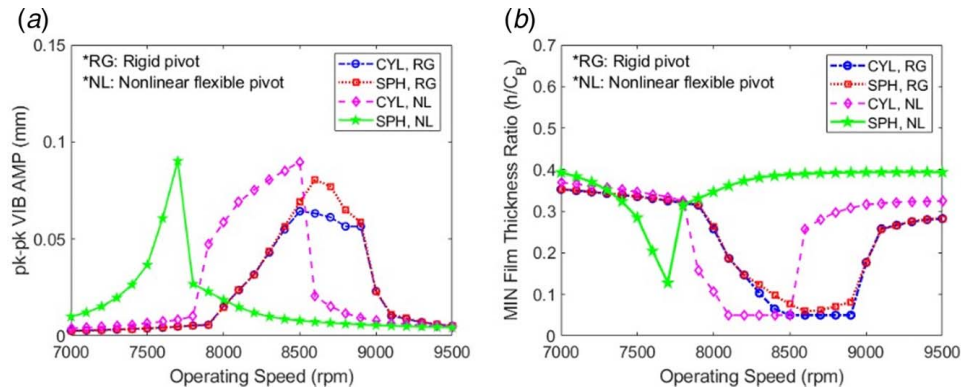
Fig. 8 Steady-state ME simulations with rigid and flexible pivots from 7000 rpm to 9500 rpm: (a) pk-pk vibration amplitude at journal and (b) minimum film thickness ratio
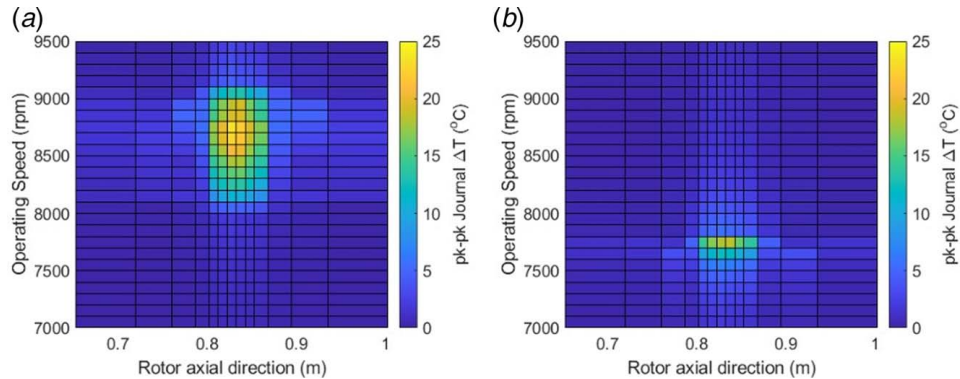

Fig. 9 Steady-state ME simulations of pk-pk journal ΔT from 7000 rpm to 9500 rpm: (a) SPH type with rigid pivot and (b) SPH type with flexible pivot

journal ΔTs occur from 8000 rpm to 9000 rpm for the rigid pivot case, and between 7600 rpm to 7800 rpm for the nonlinear, flexible pivot case. These ranges coincide with the high vibration ranges in Fig. 8(a). The similar trends of ΔT and vibration indicate that the thermal bow-related dynamic forces induced by the ΔT, cause the large vibration. A smaller pk-pk journal ΔT (max 18.4 °C) is predicted for the nonlinear, flexible pivot compared with the rigid pivot (max 23.5 °C), indicating that rigid pivot assumption may overpredict the journal ΔT and thus vibration level in ME analysis.

Transient simulations are conducted for different pivot cases in Fig. 10. At 7700 rpm, the most severe vibration level appears with the nonlinear SPH pivot with nonconverging spiral vibration in Fig. 10(a). In Fig. 10(b), the high journal ΔT is also seen to occur with fluctuating amplitudes for the identical case. Both pivot types with rigid pivots show relatively small vibration and ΔT at 7700 rpm compared with the nonlinear pivots. Meanwhile, at 8600 rpm, the rigid pivot cases exhibit more violent vibration and higher ΔT as shown in Figs. 10(c) and 10(d). These results are consistent with the steady-state results in Fig. 8 and confirms that the shift of the ME instability speed range with different pivot types.

Figure 11 shows the CYL and SPH pivot stiffness variation with time, at the 7700 rpm condition of Figs. 10(a) and 10(b). The results of only three pads are presented, since pads 4 and 5 have similar variations as pads 2 and 3. The stiffness of the CYL pivot varies from 1.55×10^9 N/m to 1.67×10^9 N/m, which is much larger than the SPH case variation, ranging from 3×10^8 N/m to 4.5×10^8 N/m in Fig. 11(b). The pivot stiffness variations mimic the vibration and ΔT variations in Figs. 10(a) and 10(b). High vibration occurs after 15 min for the nonlinear SPH pivot case shown in

Figs. 10(a) and 10(b). This increases the dynamic loading, which increases the nonlinear pivot stiffness as shown in Fig. 11(b).

Figure 12 shows transient simulation results for both the rigid and nonlinear SPH pivots at 7700 rpm. Figure 12(a) shows the vibration level is relatively small for all rotor axial locations and converges after 5 min for the rigid SPH pivot case. In contrast, the nonlinear SPH case displays nonconverging vibration even after 10 min, and especially severe vibration at the rotor's NDE end. Bearing mid-plane temperature distributions for both cases are also shown in Fig. 12(b) at time equal 30 min. The journal of the rigid SPH case shows a relatively concentric temperature distribution in Fig. 12(a), while the nonlinear SPH case exhibits an asymmetric temperature distribution in Fig. 12(b). The journal asymmetric temperature distribution causes thermal bow, which may increase net excitation level leading, to an excessive vibration level, as illustrated by Fig. 12(a).

3.4 Effect of Pivot Friction on Morton Effect. Although experimental results [33–37] confirm that the presence of pad-SPH pivot friction affects the static and dynamic performances of SPH pivot TPJBs, this effect is commonly neglected in the transient simulation for simplicity. Parametric ME studies are performed with varying SPH pivot, FC in the TPJB of the rotor model in Fig. 4. The parametric studies were not performed with CYL pivot TPJB since the contact is rolling and not sliding. The friction coefficients of the Coulomb model vary between 0.1 and 0.4. A wide range of friction coefficients from 0.1 to 0.4 were used in the simulations to present the impact of pivot friction level on the Morton effect. Results with a Stribeck friction model [40] were also obtained and the results show only minor
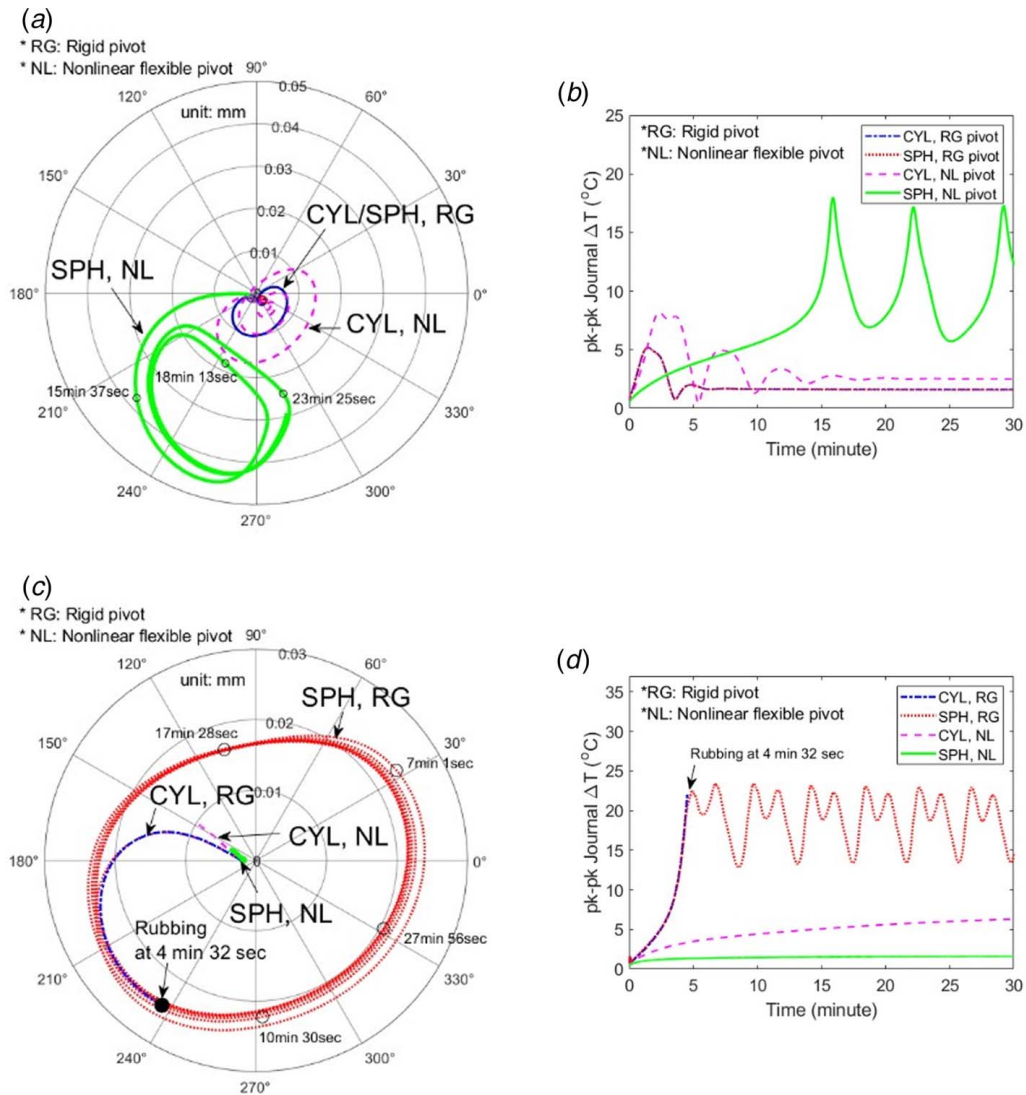
Fig. 10 Transient ME simulation at 7700 rpm and 8600 rpm: (a) 1× polar plot at 7700 rpm, (b) pk-pk journal ΔT at 7700 rpm, (c) 1× polar plot at 8600 rpm, and (d) pk-pk journal ΔT at 8600 rpm

difference with the Coulomb friction model results. Consequently, only the Coulomb friction model is used in the following study.

The SPH pivot friction, TPJB model was validated by comparison of journal static eccentricity data with experimental results [26], in Fig. 13. The simulation parameter values were identical

to those provided for the experimental rig in Ref. [26]. The journal centerline locus was generated at the operating speed of 6000 rpm with increasing bearing unit load from 0 kPa to 1896 kPa [26]. The friction coefficient between the pad and pivot is set to 0.2 since it was unknown in the reference. The simulation
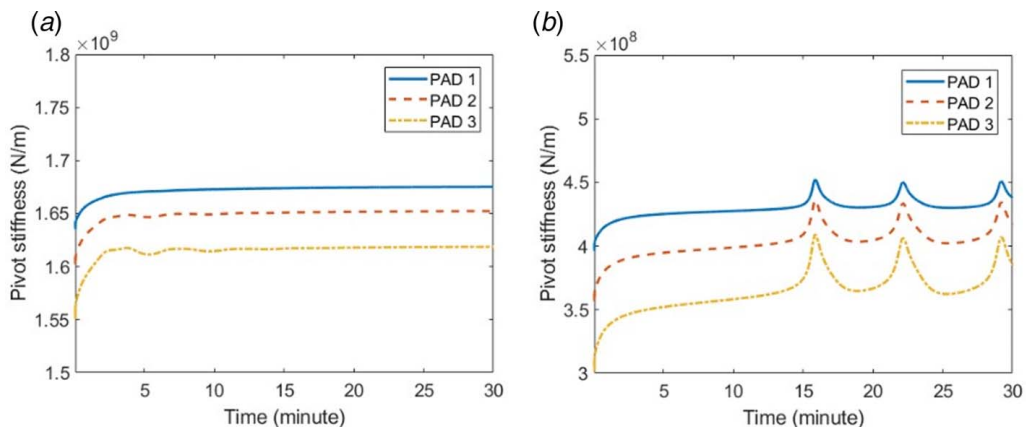

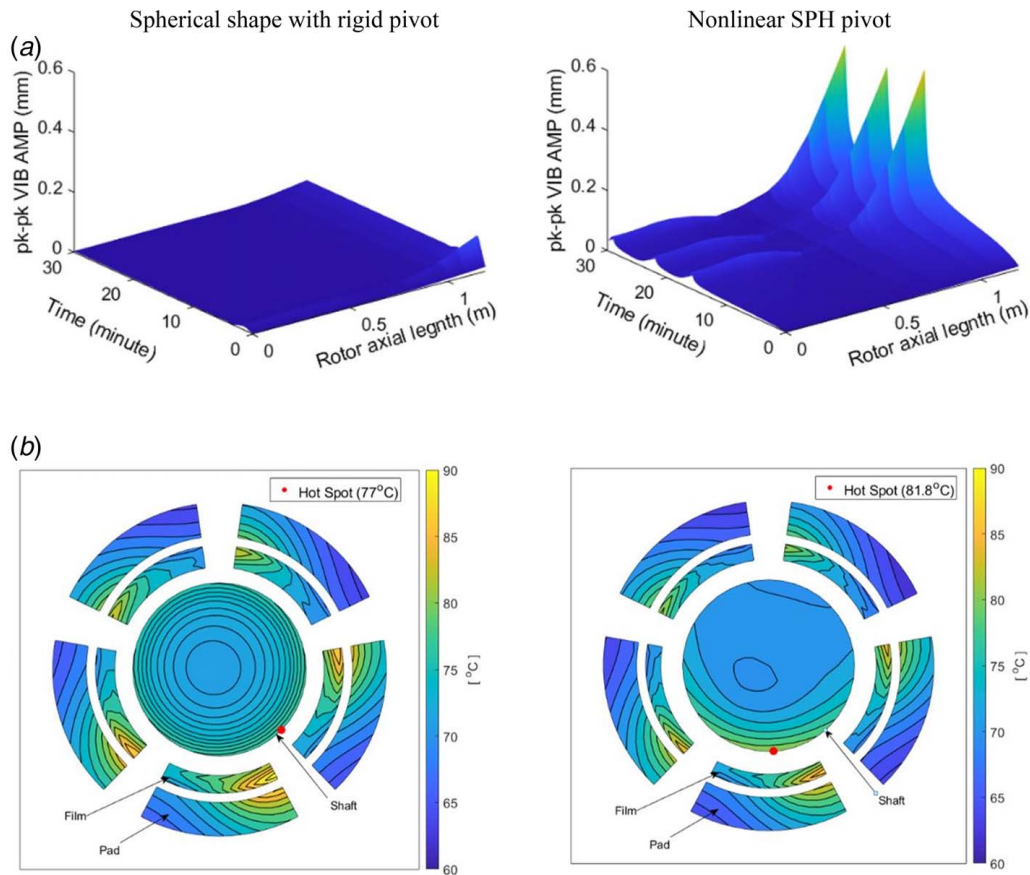**Fig. 11 Pivot stiffness versus time at 7700 rpm: (a) CYL pivot and (b) SPH pivot**

Spherical shape with rigid pivot — Nonlinear SPH pivot

Fig. 12 Transient ME simulation at 7700 rpm: (*a*) pk-pk vibration amplitude versus rotor axial position and time and (*b*) temperature distribution at bearing mid-plane at *t* = 30 min

results show that without friction the journal attitude angle is nearly zero. This greatly differs with the test results showing a large attitude angle. The predicted journal trajectory has close agreement with test results when friction is included.

Figure 14 shows nonlinear steady-state vibration responses for both the rigid and flexible pivots, considering pivot friction. The rigid pivot case in Fig. 14(*a*) shows that pivot friction significantly reduces the vibration amplitude and instability speed range of the ME. The rotor vibration amplitude at 8600 rpm is suppressed from 0.08052 mm for the no-friction case, to 0.04193 mm for the FC 0.1 case. Further increasing the friction coefficient to FC 0.3 reduces the vibration level to 0.0244 mm.

Figure 14(*a*) shows for the rigid pivot case, the rotor vibration amplitude with FC 0.4 slightly increases at 8700 rpm, compared with FC 0.2 and 0.3, while similar vibration levels occur at the other operating speeds, regardless of the FCs. Figure 14(*b*) shows for the flexible, nonlinear pivot case, pivot friction also suppresses the rotor vibration in general, but its effect on the ME vibration is not as evident as the rigid pivot case. The rigid pivot results show significant vibration reductions due to friction, both above and below the peak vibration speed (8600 rpm) of the frictionless pivot model. The flexible, nonlinear pivot results show significant vibration reductions due to friction, only below the peak vibration speed (7700 rpm) of the frictionless pivot model. The vibration actually slightly increases due to friction above that speed. The FC 0.1 provides the greatest vibration decrease for the flexible, nonlinear pivot case. The vibration level rises with increasing friction coefficients, from 0.1 to 0.4, when the speed exceeds the peak vibration speed (7700 rpm). The peak vibration speed increases with increasing friction coefficients, i.e., from 7800 rpm for FC 0.2 and 0.3, to 7900 rpm for FC 0.4. This indicates that the rigid pivot assumption may overpredict the pivot friction's vibration suppression effect on the ME

vibration. An optimal friction coefficient may exist for the pad-pivot friction, which best suppresses the rotor vibration, as demonstrated in the nonlinear pivot case in Fig. 14(*b*).

Figure 15 shows ME transient simulation results for the rigid pivot case of Fig. 14(*a*) at 8600 rpm. The spiral synchronous response shape and the journal circumferential ΔT decrease with FC 0.1, compared with the no-friction case, but do not converge. Figure 15(*b*) shows decreased settling time for ΔT with pivot
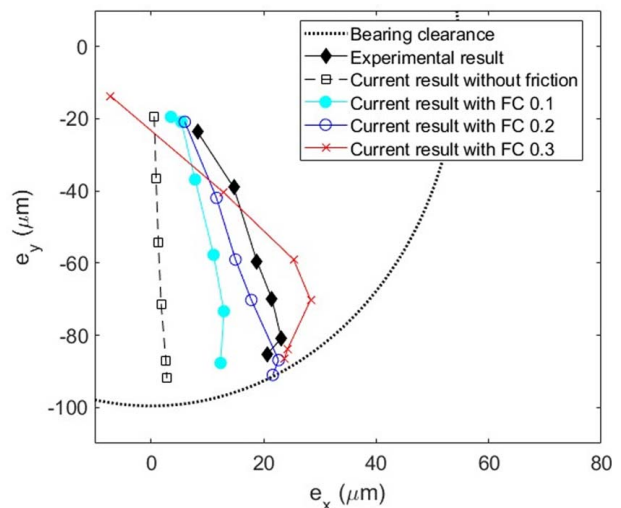

Fig. 13 Comparison of journal center locus with experimental results in Ref. [26]
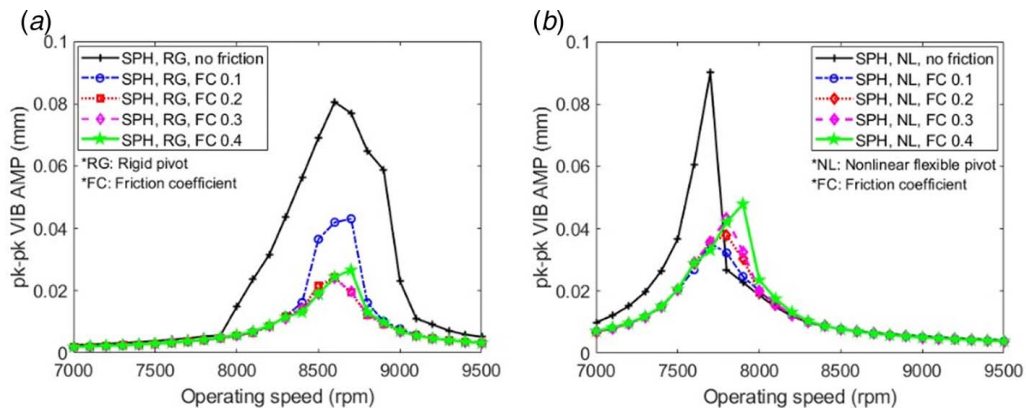
Fig. 14 Steady-state ME simulations of journal pk-pk vibration amplitude versus speed and pivot friction coefficients for (a) SPH rigid pivot model and (b) SPH flexible pivot model
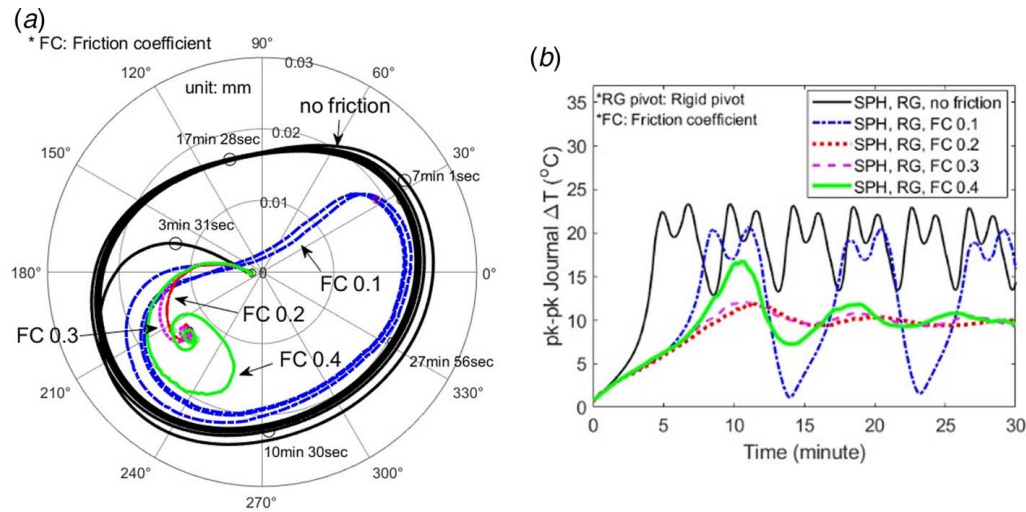

Fig. 15 Transient ME simulation of rigid pivot at 8600 rpm: (a) 1× polar plot and (b) pk-pk journal ΔT

friction, compared with the no-friction case. The 1× polar plot spiral shapes are further reduced and converge to equilibrium values with FC 0.2 and 0.3. This demonstrates the stabilizing effect of pivot friction. The journal ΔT shows reduced amplitudes and converging trajectories for FC 0.2 and 0.3 in Fig. 15(b). Further increasing the FC to 0.4, increases the trajectory of spiral synchronous vibration and ΔT, which eventually converge to values similar to the FC 0.2 and FC 0.3 cases. These results indicate the existence of an optimal level of pivot friction which most effectively suppresses the ME vibration.

Figure 16 shows the simulation results at 7700 rpm and 7900 rpm with the nonlinear pivot cases corresponding to Fig. 14(b). The FC 0.1 case shows the smallest spiral vibration in Fig. 16(a), and the shortest ΔT settling time in Fig. 16(b), at 7700 rpm. Increasing the friction coefficient up to 0.4 increases the spiral vibrations and ΔT settling time. The ΔT is slightly reduced with FC 0.2 and 0.3 but increases with FC 0.4. Conversely, the no-friction case has the most stable spiral vibration and ΔT trajectories, at 7900 rpm. These increase with increasing friction coefficients and are consistent with Fig. 14(b). The ΔT reaches 9.5 °C and 7.8 °C after 40 min and is still increasing, with FC 0.3 and 0.4. These transient simulation results confirm that for the flexible, nonlinear pivot case, pivot friction reduces the ME response below the maximum vibration speed, and increases the ME response above that speed, as demonstrated in Fig. 14(b).

Figure 17 illustrates the transient simulation results at 7900 rpm, corresponding to the orbits of the rotor at 40 min in Fig. 17(a) clearly confirm enlargement of the rotor orbits with increasing pad-pivot friction, especially at the NDE overhung side (>0.8776 m). This results from the increased thermal bow as shown in Fig. 17(b). Note that the thermal bow amplitude $\left(\sqrt{x_{bow}^2 + y_{bow}^2} \right)$ is displayed at each node in the rotor model. The bow to the left of the journal is nonzero but very small.

The bow amplitude at the NDE side (node 19) without pivot friction is 0.01135 mm, while the counterpart with FC 0.4 is about twice that value, i.e., 0.02254 mm. Figures 17(c) and 17(d) show the phase lag between high and hot spots around the journal circumference, and the bearing mid-plane temperature with FC 0.4 after 40 min, respectively. The no-friction case with relatively small vibration in Fig. 16(c) shows a stable phase lag angle response with time and converges to 8.3 deg at 40 min. The FC 0.4 case has a larger vibration, shows more fluctuations, and diminishes to the relatively small phase lag of 1.3 deg at 40 min. The high and hot spots for the FC 0.4 case are shown in Fig. 17(d). Both spots are seen to be located around 190 deg away from the 0 deg location (location of the initial mechanical imbalance) in the figure. An asymmetric temperature distribution with a high circumferential ΔT of 9.5 deg occurs with FC 0.4, while a relatively small ΔT of 4 deg occurs for the no-friction case (Fig. 16(d)). These results confirm that at 7900 rpm the pivot friction induces more asymmetric heating in the journal and increases the vibration level of the rotor.
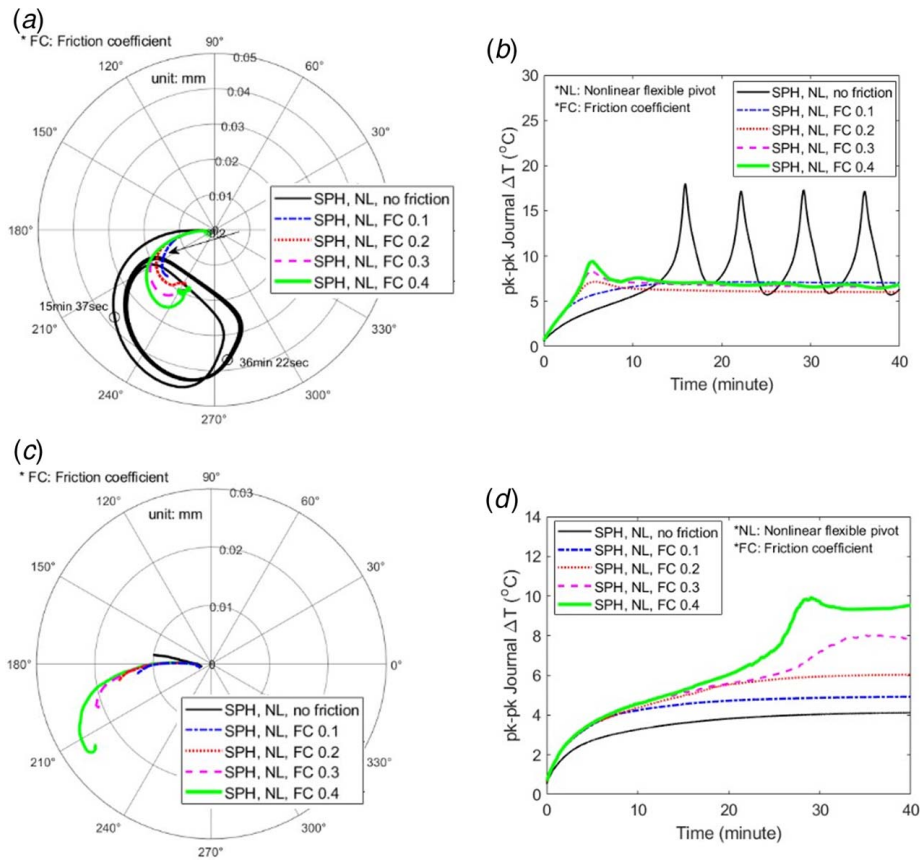
Fig. 16 Transient ME response for flexible, nonlinear pivot at 7700 rpm and 7900 rpm: (*a*) 1× polar plot at 7700 rpm, (*b*) pk-pk journal ΔT at 7700 rpm, (*c*) 1× polar plot at 7900 rpm, and (*d*) pk-pk journal ΔT at 7900 rpm
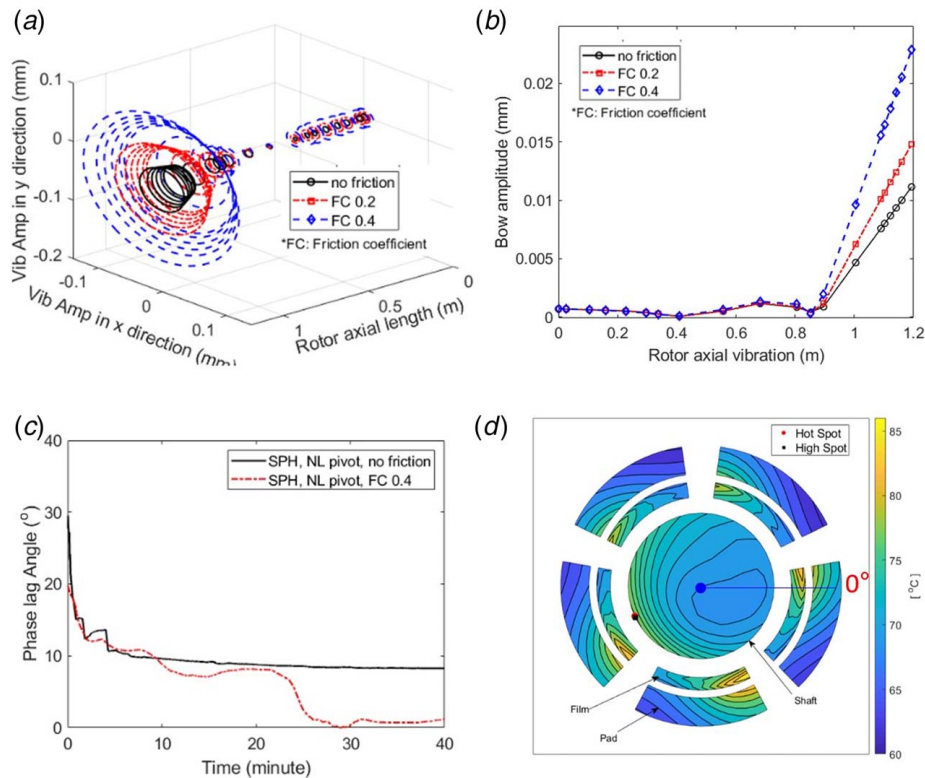

Fig. 17 Transient simulation results at 7900 rpm after 40 min: (*a*) 3D orbits of rotor, (*b*) thermal bow amplitude with different friction coefficients, (*c*) phase lag between hot and high spots, and (*d*) temperature distribution at bearing mid-plane of FC 0.4

4 Conclusions

Nonlinear ME simulations are conducted to investigate the pivot design influences on ME vibration utilizing solvers for the 3D FEM Reynolds equation, 3D Energy equation, and Euler beam models. Pivot design features such as the pivot type (CYL and SPH pivots), pivot flexibility, and pad-pivot friction are included in the TPJB models, and parametric studies are performed to investigate their effect on ME vibration level and instability speed range. Conclusions include:

(1) Spherical pivot type increases the minimum film thickness ratio compared with the CYL pivot and leads to a more symmetric temperature distribution in the axial direction due to its rolling motion. The simulation results showed that the asymmetric temperature distribution in the CYL pivot was suppressed with the SPH pivot's rolling motion. This characteristic favorably works to avoid the rubbing effect in a SPH pivot when the ME occurs.

(2) The nonlinear pivot stiffness of both CYL and SPH pivots is derived based on Hertzian contact theory. It is shown that the SPH pivots are stiffer than the CYL pivot due to its pivot geometry. The nonlinear pivot stiffness lowers the critical speed as demonstrated with a conventional rotor dynamic linear analysis. The critical speed change was larger with a spherical pivot type compared with the CYL pivot due to its stiffer pivot.

(3) The shift of the critical speed also affects the ME instability speed range and induced vibration amplitudes, as demonstrated with nonlinear transient ME simulations, including nonlinear pivot stiffness. The shift of the ME instability speed to a lower speed range, results in less severe ME vibration and journal ΔT in general.

(4) The effect of pad-pivot friction in the SPH pivot shows different trends between the rigid and nonlinear pivot cases. The effect of pivot friction on suppressing the ME is overpredicted with the rigid pivot assumption, compared with more realistic flexible, nonlinear pivots. The friction effect significantly reduces the ME instability speed range and vibration levels with the rigid pivot model. In contrast, however, the flexible, nonlinear pivot results show that pivot friction attenuates the vibration level below the speed where maximum vibration occurs and amplifies the vibration amplitude above that speed. In addition, with the flexible, nonlinear pivot, the speed where the maximum vibration level occurs is slightly shifted up with increasing friction.

(5) Vibration reduction due to the pad-pivot friction does not vary monotonically with increasing friction coefficient, and there exists an optimal value of pad-pivot friction coefficients which effectively suppresses the ME vibration.

(6) To obtain a more accurate result for a given application, a measurement of the pivot friction between the ball and housing should be made and applied in the respective simulation model.

Future works include a more sophisticated prediction method of the friction coefficients between the pad and pivot using the finite element method. The effect of the pad's flexibility on the ME vibration will be also investigated. Experimental work to verify the numerical results will be conducted.

Conflict of Interest

There are no conflicts of interest.

Data Availability Statement

The datasets generated and supporting the findings of this article are obtainable from the corresponding author upon reasonable request. The authors attest that all data for this study are included in the paper. Data provided by a third party listed in Acknowledgment. No data, models, or code were generated or used for this paper.

References

[1] Tong, X., Palazzolo, A., and Suh, J., 2017, "A Review of the Rotordynamic Thermally Induced Synchronous Instability (Morton) Effect," ASME Appl. Mech. Rev., **69**(6), p. 060801.

[2] Shin, D., Yang, J., Tong, X., Suh, J., and Palazzolo, A., 2020, "A Review of Journal Bearing Thermal Effects on Rotordynamic Response," ASME J. Tribol., **143**(3), p. 031803.

[3] de Jongh, F. M., and Morton, P. G., 1996, "The Synchronous Instability of a Compressor Rotor Due to Bearing Journal Differential Heating," ASME J. Eng. Gas Turbines Power, **118**(4), pp. 816–824.

[4] de Jongh, F., and Van Der Hoeven, P., 1998, "Application of a Heat Barrier Sleeve to Prevent Synchronous Rotor Instability," 27th Turbomachinery Symposium, College Station, TX, pp. 17–26.

[5] Keogh, P. S., and Morton, P. G., 1993, "Journal Bearing Differential Heating Evaluation With Influence on Rotor Dynamic Behaviour," Proc. R. Soc. London, Ser. A, **441**(1913), pp. 527–548.

[6] Keogh, P., and Morton, P., 1994, "The Dynamic Nature of Rotor Thermal Bending Due to Unsteady Lubricant Shearing Within a Bearing," Proc. R. Soc. London, Ser. A, **445**(1924), pp. 273–290.

[7] Lee, J. G., and Palazzolo, A., 2012, "Morton Effect Cyclic Vibration Amplitude Determination for Tilt Pad Bearing Supported Machinery," ASME J. Tribol., **135**(1), p. 011701.

[8] Suh, J., and Palazzolo, A., 2014, "Three-Dimensional Thermohydrodynamic Morton Effect Simulation—Part I: Theoretical Model," ASME J. Tribol., **136**(3), p. 031706.

[9] Suh, J., and Palazzolo, A., 2014, "Three-Dimensional Thermohydrodynamic Morton Effect Analysis—Part II: Parametric Studies," ASME J. Tribol., **136**(3), p. 031707.

[10] Tong, X., Palazzolo, A., and Suh, J., 2016, "Rotordynamic Morton Effect Simulation With Transient, Thermal Shaft Bow," ASME J. Tribol., **138**(3), p. 031705.

[11] Tong, X., and Palazzolo, A., 2016, "Double Overhung Disk and Parameter Effect on Rotordynamic Synchronous Instability—Morton Effect—Part I: Theory and Modeling Approach," ASME J. Tribol., **139**(1), p. 011705.

[12] Tong, X., and Palazzolo, A., 2016, "Double Overhung Disk and Parameter Effect on Rotordynamic Synchronous Instability—Morton Effect—Part II: Occurrence and Prevention," ASME J. Tribol., **139**(1), p. 011706.

[13] Tong, X., and Palazzolo, A., 2018, "Tilting Pad Gas Bearing Induced Thermal Bow Rotor Instability," Tribol. Int., **121**, pp. 269–279.

[14] Tong, X., and Palazzolo, A., 2017, "Measurement and Prediction of the Journal Circumferential Temperature Distribution for the Rotordynamic Morton Effect," ASME J. Tribol., **140**(3), p. 031702.

[15] Shin, D., and Palazzolo, A. B., 2020, "Tilting Pad Journal Bearing Misalignment Effect on Thermally Induced Synchronous Instability (Morton Effect)," ASME J. Tribol., **143**(3), p. 031802.

[16] Shin, D., Palazzolo, A. B., and Tong, X., 2020, "Squeeze Film Damper Suppression of Thermal Bow-Morton Effect Instability," ASME J. Eng. Gas Turbines Power, **142**(12), p. 121013.

[17] Childs, D. W., and Saha, R., 2012, "A New, Iterative, Synchronous-Response Algorithm for Analyzing the Morton Effect," ASME J. Eng. Gas Turbines Power, **134**(7), p. 072501.

[18] Murphy, B. T., and Lorenz, J. A., 2010, "Simplified Morton Effect Analysis for Synchronous Spiral Instability," ASME J. Vib. Acoust., **132**(5), p. 051008.

[19] Kellenberger, W., 1980, "Spiral Vibrations Due to the Seal Rings in Turbogenerators Thermally Induced Interaction Between Rotor and Stator," ASME J. Mech. Des., **102**(1), pp. 177–184.

[20] Kirk, G., Guo, Z., and Balbahadur, A., 2003, "Synchronous Thermal Instability Prediction for Overhung Rotors," 32nd Turbomachinery Symposium, Houston, TX, Sept. 8–11, pp. 121–135.

[21] Eckert, L., and Schmied, J., 2008, "Spiral Vibration of a Turbogenerator Set: Case History, Stability Analysis, Measurements and Operational Experience," ASME J. Eng. Gas Turbines Power, **130**(1), p. 012509.

[22] Suh, J., and Choi, Y., 2016, "Pivot Design and Angular Misalignment Effects on Tilting Pad Journal Bearing Characteristics: Four Pads for Load on Pad Configuration," Tribol. Int., **102**, pp. 580–599.

[23] Gadangi, R. K., Palazzolo, A. B., and Kim, J., 1996, "Transient Analysis of Plain and Tilt Pad Journal Bearings Including Fluid Film Temperature Effects," ASME J. Tribol., **118**(2), pp. 423–430.

[24] San Andrés, L., and Tao, Y., 2013, "The Role of Pivot Stiffness on the Dynamic Force Coefficients of Tilting Pad Journal Bearings," ASME J. Eng. Gas Turbines Power, **135**(11), p. 112505.

[25] Dang, P. V., Chatterton, S., and Pennacchi, P., 2019, "The Effect of the Pivot Stiffness on the Performances of Five-Pad Tilting Pad Bearings," Lubricants, **7**(7), p. 61.

[26] Childs, D., and Harris, J., 2009, "Static Performance Characteristics and Rotordynamic Coefficients for a Four-Pad Ball-in-Socket Tilting Pad Journal Bearing," ASME J. Eng. Gas Turbines Power, **131**(6), p. 062502.

[27] Kulhanek, C. D., and Childs, D. W., 2012, "Measured Static and Rotordynamic Coefficient Results for a Rocker-Pivot, Tilting-Pad Bearing With 50 and 60% Offsets," ASME J. Eng. Gas Turbines Power, **134**(5), p. 052505.

[28] Mehdi, S. M., Jang, K., and Kim, T., 2018, "Effects of Pivot Design on Performance of Tilting pad Journal Bearings," Tribol. Int., **119**, pp. 175–189.

[29] Young, W. C., 1989, *Roark's Formulas for Stress & Strain*, 6th ed., McGraw-Hill, New York.

[30] Kirk, R. G., and Reedy, S. W., 1988, "Evaluation of Pivot Stiffness for Typical Tilting-Pad Journal Bearing Designs," ASME J. Vib. Acoust. Stress Reliab., **110**(2), pp. 165–171.

[31] Nicholas, J. C., and Wygant, K. D., 1995, "Tilting Pad Journal Bearing Pivot Design For High Load Applications," Proceedings of the 24th Turbomachinery Symposium, Houston, TX, pp. 33–47.

[32] Shi, Z., Jin, Y., and Yuan, X., 2019, "Influence of Pivot Design on Nonlinear Dynamic Analysis of Vertical and Horizontal Rotors in Tilting pad Journal Bearings," Tribol. Int., **140**, p. 105859.

[33] Wygant, K. D., Barrett, L. E., and Flack, R. D., 1999, "Influence of Pad Pivot Friction on Tilting-Pad Journal Bearing Measurements—Part I: Steady Operating Position," Tribol. Trans., **42**(1), pp. 210–215.

[34] Wygant, K. D., Barrett, L. E., and Flack, R. D., 1999, "Influence of Pad Pivot Friction on Tilting-Pad Journal Bearing Measurements—Part II: Dynamic Coefficients," Tribol. Trans., **42**(1), pp. 250–256.

[35] Pettinato, B., and De Choudhury, P., 1999, "Test Results of Key and Spherical Pivot Five-Shoe Tilt Pad Journal Bearings Part I: Performance Measurements," Tribol. Trans., **42**(3), pp. 541–547.

[36] Pettinato, B., and De Choudhury, P., 1999, "Test Results of Key and Spherical Pivot Five-Shoe Tilt Pad Journal Bearings Part II: Dynamic Measurements," Tribol. Trans., **42**(3), pp. 675–680.

[37] Sabnavis, G., 2005, "Test Results for Shaft Tracking Behavior of Pads in a Spherical Pivot Type Tilting Pad Journal Bearing," M.S. thesis, Virginia Polytechnic Institute and State University, Blacksburg, VA.

[38] Kim, S., and Kim, K., 2008, "Influence of Pad Pivot Friction on Tilting Pad Journal Bearing," Tribol. Int., **41**(8), pp. 694–703.

[39] He, F., 2017, "Including Pivot Friction in Pad Motion for a Tilting Pad Journal Bearing With Ball-Socket Pivots," ASME Proceedings, Turbo Expo 2017: Turbomachinery Technical Conference and Exposition, Charlotte, NC, June 26–30, p. V07AT34A036.

[40] Kim, S., and Palazzolo, A. B., 2019, "Pad–Pivot Friction Effect on Nonlinear Response of a Rotor Supported by Tilting-Pad Journal Bearings," ASME J. Tribol., **141**(9), p. 091701.

[41] Lu, X., Khonsari, M. M., and Gelinck, E. R. M., 2006, "The Stribeck Curve: Experimental Results and Theoretical Prediction," ASME J. Tribol., **128**(4), pp. 789–794.

[42] Heinrich, J., Huyakorn, P., Zienkiewicz, O., and Mitchell, A., 1977, "An 'Upwind' Finite Element Scheme for Two-Dimensional Convective Transport Equation," Int. J. Numer. Methods Eng., **11**(1), pp. 131–143.